RESEARCH ARTICLE
SOLID EARTH: SEISMOLOGY

Earth and Planetary Physics
9: 212–224, 2025
doi: 10.26464/epp2025020

Research on the three-dimensional electrical structure of the shallow portion of the southern segment of the Red River Fault (Dazhai Village)

Jiong Zhang[1], Yan Jing[1], XiaoBin Chen[1*], JunTao Cai[1], ZhongYin Liu[1], XingXing Huang[1], and PeiJie Wang[2]

[1]Key Laboratory of Compound and Chained Natural Hazards Dynamics, Ministry of Emergency Management of China; National Institute of Natural Hazards, Ministry of Emergency Management of China, Beijing 100085, China;

[2]Department of Earth and Space Sciences, Southern University of Science and Technology, Shenzhen 518055, China

Key Points:

- Three-dimensional electrical structures within the southern segment of the Red River fault zone were identified using BBMT and AMT data collected along traverses across this region.
- The southern segment of the Red River fault is a boundary with high and low resistivity.
- High-resolution electrical structures were utilized to accurately delineate the fault's geometric characteristics in the southern segment of the Red River fault zone.

Citation: Zhang, J., Jing, Y., Chen, X. B., Cai, J. T., Liu, Z. Y., Huang, X. X., and Wang, P. J. (2025). Research on the three-dimensional electrical structure of the shallow portion of the southern segment of the Red River Fault (Dazhai Village). *Earth Planet. Phys.*, *9*(2), 212–224. http://doi.org/10.26464/epp2025020

Abstract: No earthquake of magnitude six or greater has been recorded historically in the southern segment of the Red River Fault (RRF). This absence constitutes a significant seismic gap, suggesting a risk of future strong earthquakes. The China Earthquake Science Experimental Site intends to conduct drilling exploration in this area, which necessitates improved knowledge of the fault zone's geometric distribution characteristics and deep structure. We obtained and analyzed audio and broadband magnetotelluric (MT) data collected at one of the alternative drilling stations (in the Dazhai Village of Honghe County). We have used these data to obtain a high-resolution 3-D electrical model of this study area's subsurface to a depth of 5 km. We report that the electrical structure from the surface to 0.5 km is relatively complex, characterized by alternating high and low resistivity; below 0.5 km, the electrical structure becomes more simplified. The RRF extends northwest–southeast orientation along the high and low resistivity boundary, dipping northeastward. The electrical structure of the Red River Valley, which the fault zone traverses, reveals low resistivity characteristics with a lateral width of up to 2 km. This study offers critical electromagnetic constraints that enhance our understanding of the tectonic characteristics of the RRF. The findings will inform and aid in the design of drilling plans for the southern segment of the RRF region.

Keywords: the southern segment of the Red River Fault; electrical structure; magnetotellurics

1. Introduction

The Red River Fault (RRF), extending approximately 1000 km (approximately 600 km within China), represents a significant large-scale strike-slip fault in the southwestern part of China. As the boundary between the Indochina block and the Yangtze block, the RRF zone has undergone multiple phases of tectonic deformation since the Cenozoic era (Figure 1a). Initially, it functioned as the main boundary of the northward extrusion of the Tibetan Plateau, exhibiting large-scale left-lateral strike-slip motion. However, since the Miocene epoch the deformation characteristics of the RRF have transitioned to right-lateral strike-slip motion from the original left-lateral, persisting to the present day (Tapponnier et al., 1990, 2001; Ji SC et al., 2008; Xu ZQ et al., 2011). Therefore, it is crucial to investigate the current seismic activity and tectonic deformation mechanisms of the RRF zone to understand the evolution of tectonic processes in the southeastern margin of the Tibetan Plateau, a topic that has garnered significant attention in recent decades (Guo SM et al., 2001; Hao TY et al., 2005; Zhang JJ et al., 2006; Wang FY et al., 2014).

Based on distinct differences in structural and geomorphological features, geometrics, and seismic activity, the RRF is categorized into three segments from north to south (Figure 1b): north (Eryuan to Midu), middle (Juli to Dadoumen), and south (Chunyuan to Hekou). The north segment is the tensile region at the tail end of the strike-slip fracture; the middle and southern segments are in the shear deformation region with horizontal movement. The seismicity of the RFF's southern segment is disputed. One view is

First author: J. Zhang, s060872@163.com
Correspondence to: X. B. Chen, cxb@pku.edu.cn
Received 15 OCT 2024; Accepted 12 JAN 2025.
First Published online 04 MAR 2025.

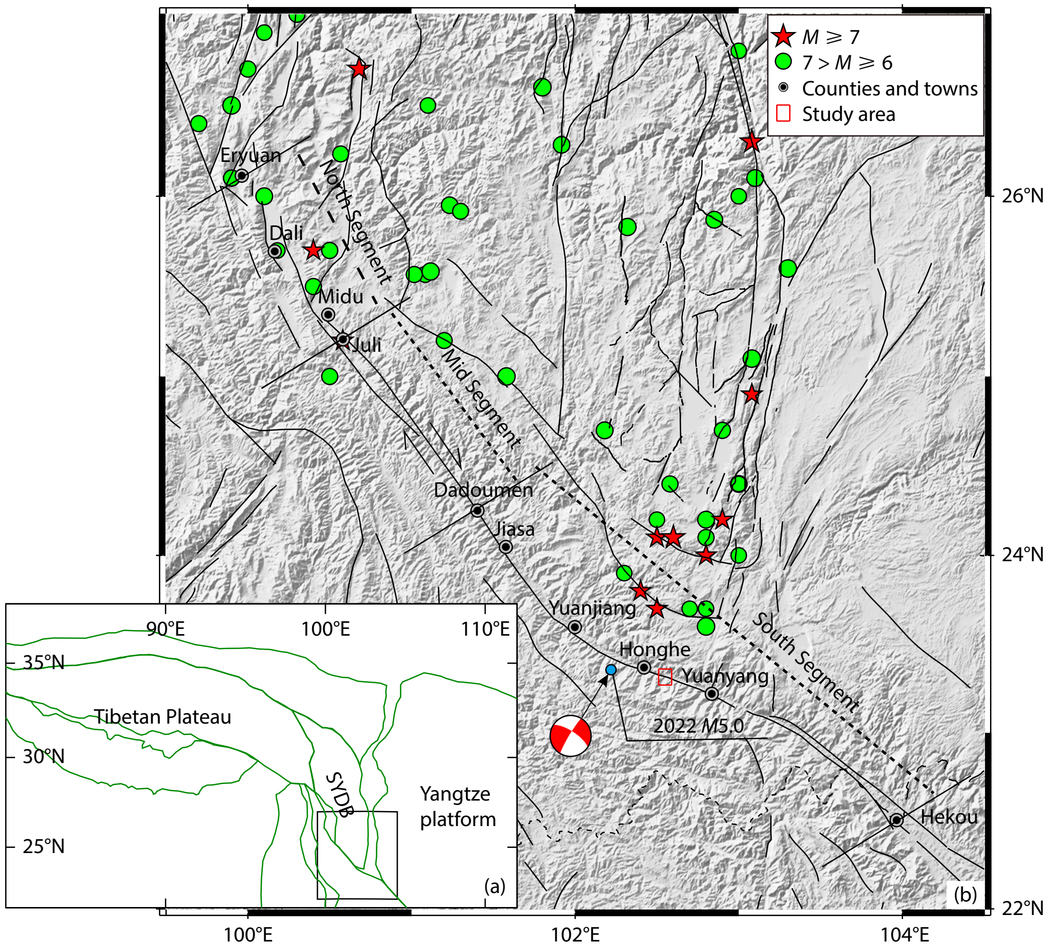

Figure 1. Schematic tectonic setting surrounding the study area (which is outlined in red). (a) Regional map of the Sichuan–Yunnan Diamond-shaped Block (SYDB) and adjacent regions. Green lines denote tectonic boundaries of mainland China. (b) Tectonics and seismicity in the Red River fault and adjacent region surrounding the study area. Red stars show $M > 7$ earthquakes; green circles show earthquakes between $M6$ to $M7$; the blue circle locates the $M5.0$ Honghe quake (from https://www.ceic.ac.cn/). Black and gray circles represent major counties and towns in Yunnan. The focal mechanisms shown here originate from GCMT (https://www.globalcmt.org/). The fault data come from Xu XW et al. (2016); the tectonic block data are from Zhang PZ et al. (2003).

that an apparent seismic void in the southern segment's history indicates that the block boundary action has been weakening there, making major earthquakes very unlikely in that segment (Guo SM et al., 2001; Zhang JG et al., 2009). The other view is that the southern segment may still be in a seismogenic condition, characterized by a long earthquake recurrence period, and thus may remain at risk of significant earthquakes (Allen et al., 1984; Li X et al., 2016; Wen XZ et al., 2022). Additionally, the dip of the RRF zone is in dispute. Geological survey results indicate that the fault dip is oriented to the northeast (Zhang JJ et al., 2006; Li X et al., 2016). The results of magnetotelluric imaging reveal that the southwest side of the RRF zone is a high-resistivity body, and the northeast side includes a low-resistivity body of a certain scale (Yu N et al., 2020; Ye T et al., 2022). Thus, consistent with the geological survey results, the primary segment of the fault zone presents a shallow near-vertical and deep NE-dipping geometry. However, the seismological results reveal that the southwest side of the RRF is a low-velocity body, and the northeast side is a high-speed body; the main section tends to incline southwestward (Wang FY et al., 2014; Chen SW et al., 2016; Wen XZ et al., 2022). More research is imperative on the southern segment of the RRF zone as the seismic risk and geometric characteristics on either side of the fault zone remain subjects of contention.

The magnetotelluric (MT) method is a natural electromagnetic field technique that was independently proposed by Tikhonov (1950) and Cagniard (1953) during the early 1950s. According to different measurement frequencies, MT can be categorized into audio MT (AMT), broadband MT (BBMT), and long-period MT (LMT). MT is effective for imaging shallow and crustal structures associated with active faults (Becken et al., 2011; Sun XY et al., 2020; Cai JT et al., 2023) and geothermal exploration in volcano areas (Gao J et al., 2020; Yamaya et al., 2022), and for constraining lithospheric rheology (Unsworth et al., 2005; Liu LJ and Hasterok, 2016). In practical applications, combinations of AMT+BBMT or BBMT+LMT have been employed to fulfill the requirements for multi-scale exploration regarding target depth and resolution.

This paper requires both a high-resolution structure in the shallow part (suitable for AMT) and a depth of 5 km (suitable for MT). We utilize a multi-scale and multi-period exploration method (Liu ZY et al., 2023) to characterize the location of one of the drilling alternative stations in the southern segment of the RRF (Dazhai village). We used BBMT and AMT data to constrain the 3-D electrical structure at a depth of 5 km in this location within the southern segment of the RRF. Our results make it possible to deduce new insight into the kinematic and geometric characteristics of the RRF, providing a scientific basis for understanding the active structural characteristics of the southern segment of the RRF, including likely seismic activity especially at the drilling location.

2. Geological Background

The RRF is a boundary tectonic belt on the southeastern margin of the Tibetan Plateau, with the South China block on its east side and the Indochina block on its west side. Since the Quaternary, the average slip rate of the RRF zone has been 2–5 mm/a (Allen et al., 1984; Replumaz et al., 2001; Schoenbohm et al., 2006). Nine moderate earthquakes with $M \geq 6$ have been recorded in the RFF, all of them concentrated in its northern segment (Li X et al., 2016). In contrast, historical records note no $M \geq 6$ quakes in the southern segment of the RRF. The fault zone's different segments also show uneven earthquake distribution in time and space (Guo SM et al., 2001; Li X et al., 2016; Wen XZ et al., 2022). On November 19, 2022, an *M*5.0 earthquake occurred at the southern segment of the RRF, with epicenter location 102.26°E, 23.37°N. Coulomb stress analyses of historical major earthquakes in the southern segment of the RRF Zone demonstrate necessitating vigilance towards persistent seismic hazard potential (Wang MC et al., 2024). Li et al. (2016) concluded that the southern segment of the RRF exhibited geological evidence of seismic activity during the Holocene. Explicit seismic activity occurred in the middle and late Holocene, but the recurrence period was very long; thus is it possible that we may again be in the long period before the next large earthquake. Combining the quantitative parameters of existing active faults and the evanescent rate of ancient earthquakes, Xu XW et al. (2017) defined the Nanjian–Yuanyang area along the Red River as a potential high-magnitude seismogenic fault. The major rocks of the RRF and surrounding region are also very complex. The southwest side of the RRF consists mainly of Proterozoic metamorphic rock; the area traversed by the RRF zone is predominated composed of the Cenozoic sandstone; the northeast side of the RRF is Paleozoic metamorphic rock and Mesozoic mudstone (Figure 2). Therefore, we agree that large earthquakes are likely to occur in the southern segment of RRF. It is therefore of great academic and practical value to learn more about the crustal electrical structure of the southern segment of the RRF.

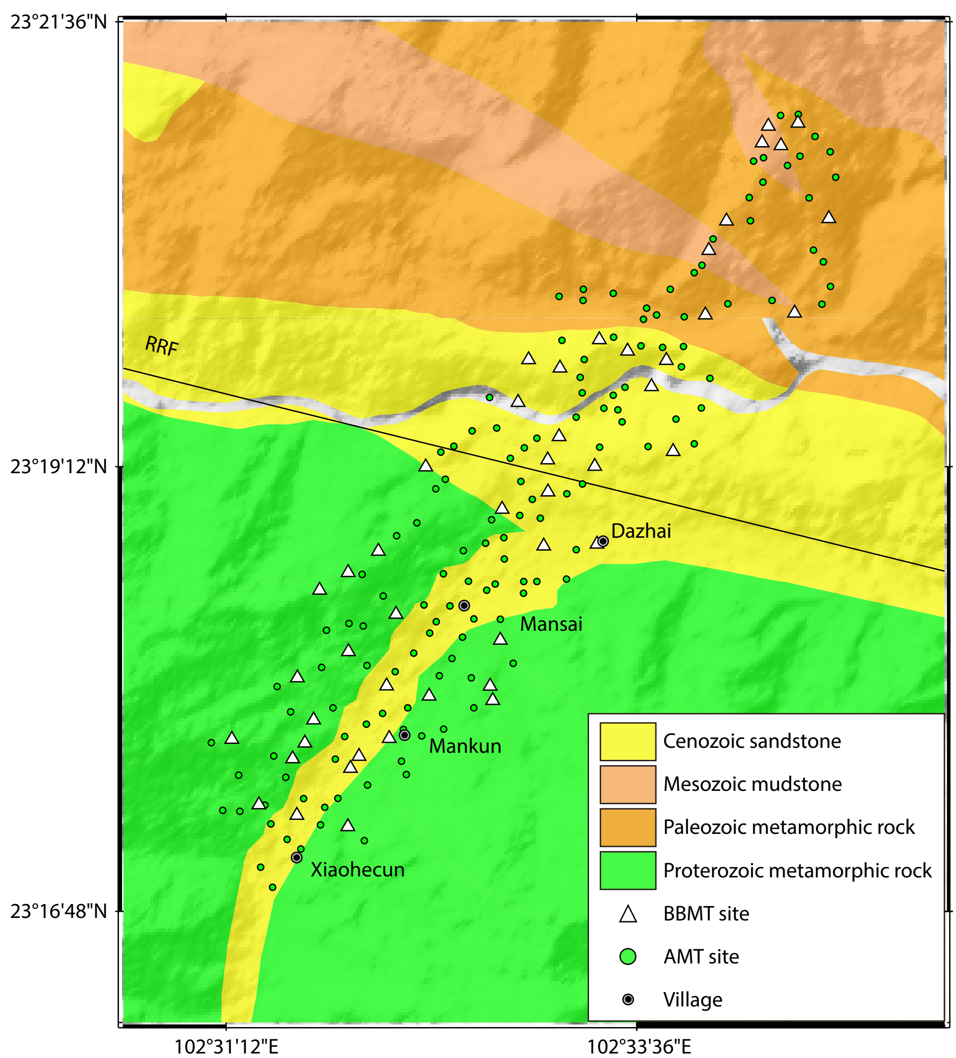

Figure 2. Geological map of the study area, indicating primary rock types and locations of the BBMT and AMT sites.

3. Data Acquisition

In March 2023, we conducted a field survey in the southern segment of the RRF and adjacent region. The survey area environment is very complicated — crisscrossed rivers, exposed bedrock, electromagnetic noise from high-voltage transmission lines. These conditions were a great challenge in obtaining high-quality original data. We rejected use of a 2-D profile observation scheme, given the complex topography of the region's mountains, rivers, and forests. Instead, we adopted a 3-D array observation scheme that had been used in constructing the Kangding tunnel on the Sichuan–Tibet Railway (Zhang J et al., 2022). In order to ensure the acquisition of high-quality data during our field observations, we imported into Google Earth software the road information from the Kanding field survey and then referred to the topographic and geomorphological design of the observed sites.

The area we studied in the southern RRF (Dazhai village) is delineated as a narrow strip measuring 8 km × 2 km, with its narrow side aligned along the strike direction of the fault zone and its long side following the vertical fault trend (Figure 2). This area crosses Xiaohe Village, Mankun Village, Manzhai Village, and Dazhai Village. This study implemented a novel methodology (Liu ZY et al., 2023), employing a hybrid field observation scheme integrating AMT and BBMT. We designed the AMT station spacing of approximately 200 m to achieve high-resolution of the shallow part, and the BBMT station spacing of approximately 1 km to achieve exploration down deeper, to 5 km. AMT and BBMT data were acquired using the MTU-5A system (Phoenix Geophysics Ltd.). We measured the two horizontal components (E_x and E_y) of the electric field and two orthogonal components (H_x and H_y) of the magnetic field using MTC-150 induction coils. To ensure high-quality data at each station the recording time for the AMT surveys was more than 0.5 h; for the BBMT surveys it was more than 4 h. The time series data for the four measured components were processed using the SSMT2000 software (Phoenix Geophysics Ltd.). After data processing, we calculated apparent resistivity and impedance phase values at 46 BBMT sites (frequency range 0.00084–10000 Hz) and 131 AMT sites (frequency range 1–10,000 Hz).

4. MT Data Analysis

Rose diagrams (Figure 3) are plotted with strike angles produced by the conjugate impedance method (Cai JT et al., 2010) weighted by the two-dimensional effective factor (Chen XB et al., 2014) of data collected within four different frequency bands. Figure 3a presents the statistical rose petal based on data in the 1000–10,000 Hz frequency band. This diagram displays a disorganized pattern: largest petals are NW-SE or nearly EW, the former being (by a slim margin) the rose's electrical principal axis. Both of these directions deviate from the main tectonic strike of the RRF. The main reason for this phenomenon may be that the shallow part of the survey area is affected by terrain-cutting, making it impossible to detect the principal orientation at all frequencies.

However, interpretation of the rose petals based on data in the 100–1000 Hz band (Figure 3b) is more straightforward; the rose petals here are broader, but still suggest that the linear structure in the study area is very complicated.

In the frequency bands of 10–100 Hz (Figure 3c) and 1–10 Hz (Figure 3d), the rose petals are more organized; by a narrow margin the electrical principal axis is close to NWW-SEE. These relatively narrow rose petals in the low-frequency bands suggest that the linear structural characteristics in the study area are relatively simple, consistent with the trend observed in surface investigation of active faults in the RRF zone. But there is a 90° ambiguity in the direction of the principal axis.

Based on the one-dimensional deviation, two-dimensional deviation, and the best principal axis azimuth angle obtained from the impedance tensor decomposition, and considering the 90° ambiguity of the strike angle, we propose the tensor decomposition bi-orthogonal diamond diagram. The drawing method is as follows: a 1-D deviation is used to represent the long axis of the diamond, and a 2-D deviation is used to represent the short axis of the diamond. The orientation of the long axis is the orientation of the best principal axis, forming a tensor decomposition diamond diagram. Due to the 90° ambiguity, after rotating the diamond by 90°, the polygon formed by the superposition of the double diamonds are the bi-orthogonal diamond diagram. If the bi-orthogonal diamond is small, it indicates that the area is 1-D media. Otherwise, if the bi-orthogonal diamond is sharp, it indicates that the area is 2-D media. If the bi-orthogonal diamond is fat, it indicates that the area is 3-D media. The interior of the polygon can be filled with the color of resistivity, phase, 2-D effective factor and other parameters. It can be seen that the bi-orthogonal diamond diagram comprehensively displays the 1-D deviation, 2-D deviation, the orientation of the best principal axis, and another parameter obtained from the tensor decomposition. Compared with the phase tensor ellipse (Caldwell et al., 2004), it provides more information.

In Figure 4, the colors correspond to the phases of the impedance invariant Z_4, where $Z_4 = (Z_{xy} - Z_{yx})/2$. Additionally, the phase is subject to minor local distortions, which more effectively reflect variations in the resistivity of underground media.

Figure 4 presents bi-orthogonal diamond diagrams derived from tensor decomposition in different frequencies (specifically, 900 Hz, 115 Hz, 11.2 Hz, and 1.02 Hz). At 900 Hz, tensor decomposition results (Figure 4a) reveal that the linear structure is significant in the northeast of the survey area; several dispersed survey points exhibit 3-D characteristics in the southwest of the survey area. We suggest that these points are associated with uneven development of shallow geological structures. Tensor decomposition results (Figure 4b) at the frequency of 115 Hz indicate that the overall 2-D linearity is further enhanced under the RRF zone, suggesting that the northwest–westward linear feature, with its linear structural characteristics, is strongly consistent with the linear feature of known fault structures. In the low frequency band of 1.02–11.2 Hz, the 2-D linear characteristics are gradually weakened; 3-D characteristics now occupy the main position (Figure 4c–d).

Phase value analysis of the fill impedance invariant Z_4 reveals that the area within the survey zone exhibits a northeast high-phase and southwest low-phase feature. In the localized region where the blocks on both sides of the RRF interact, there is an alternating

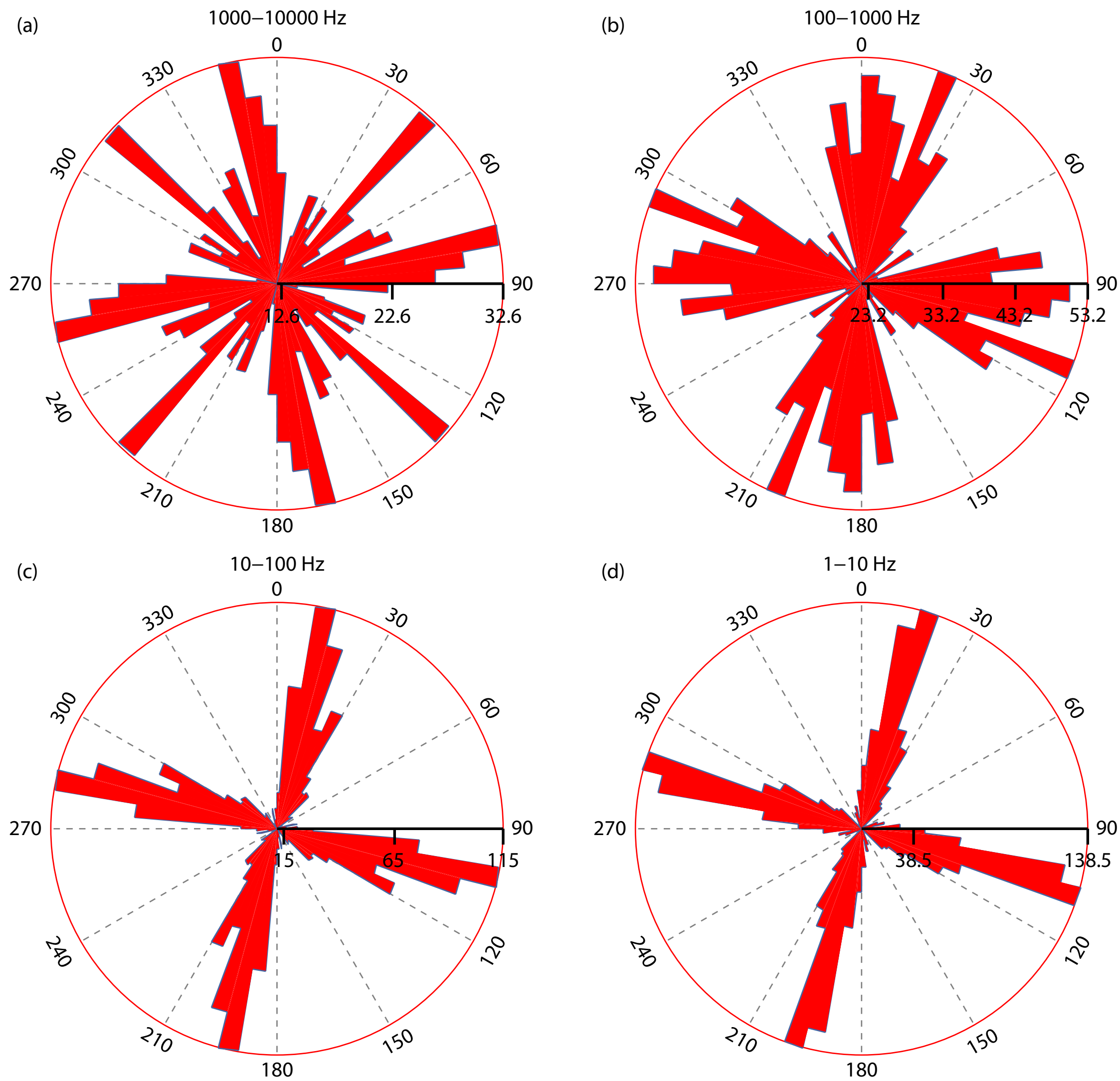

Figure 3. Rose diagrams plotted with decomposition results in four frequency bands. (a) 1000–10,000 Hz, (b) 100–1000 Hz, (c) 10–100 Hz, (d) 1–10 Hz. Red wedges indicate two possible strike directions, reflecting a 90° ambiguity in the decomposition results.

pattern of high and low phases. The electrical characteristics of the area we have studied, which passes through the RRF, are generally complex. Only 3-D inversion incorporating details of this terrain can provide a relatively reliable electrical structure model.

5. 3-D Inversion and Results

5.1 3-D MT Inversion

Three-dimensional magnetotelluric inversion technology has become widely used in scientific research fields since 2010, when introduction of ModEM programs (Egbert and Kelbert, 2012; Kelbert et al., 2014) greatly reduced memory requirements and improved inversion speeds. 3-D inversion calculation is implemented on the toPeak software system (Liu ZY et al., 2022). We selected the second generation ModEM ADORA program to be integrated into the software used for the inversion calculations in this research (Liu ZY et al., 2024). Due to the large amount of computation involved in 3-D inversion, our calculations were carried out on the computing platform of the Beijing Super Cloud Center.

Before the 3-D inversion, we utilized the MTP software to rotate the MT data to the best data quality one by one and deleted the bad data simultaneously. The Rhoplus fitting (Parker and Booker, 1996) is adoped as the reference basis for judging the data quality. The MT 3-D inversion algorithm of arbitrary data orientation angles allows for direct inversion of observations with different coordinate orientation angles (Liu ZY et al., 2024).

Due to the significant terrain relief in the survey area, three-dimensional terrain inversion is necessary to obtain a reliable electrical structure model. In this paper, national 30m-precision DEM data are is used to build a terrain file in the research area (Figure. 5a).

The process of 3-D inversion was divided into two steps. First, the low-frequency and coarse mesh three-dimensional inversion calculation was carried out for each BBMT measuring point. The inversion grid design was as follows: the grids were set as 31 × 64 × 70 nodes in the *x*-, *y*-, and *z*-directions. The grid spacing in the *x* and *y* directions was 200 m; the grid number was 10 extended grids in each direction; the grid spacing increase was by

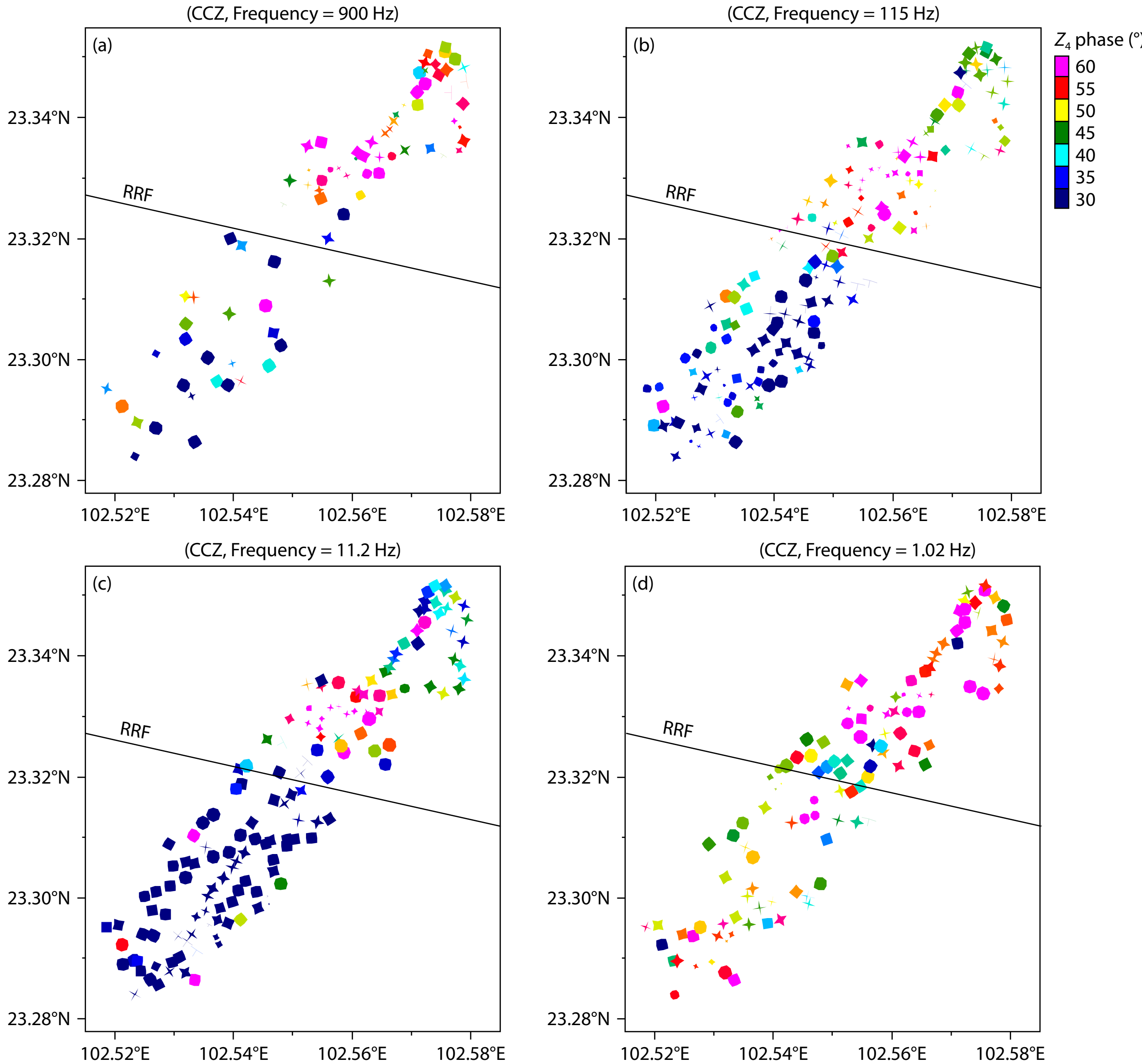

Figure 4. Tensor decomposition bi-orthogonal diamond diagrams in different frequencies. (a) 900 Hz, (b) 115 Hz, (c) 11.2 Hz, (d) 1.02 Hz. The colors represent phases of the impedance invariant Z_4.

a proportionality factor of 1.75. The thickness of the first layer in the *z* direction was 50 m and extended down to 75,119 m after 1700 m in accordance with the previous step increases of a factor of 1.2. There were 46 BBMT measurement points involved in the inversion calculation; the number of frequencies used for inversion was 30; the frequency range was 0.00084–18.8 Hz; the inversion data were selected by apparent resistivity (R_{xy} and R_{yx}) and impedance phase (P_{xy} and P_{yx}). The error floor of the apparent resistivity was set to 5%, and that of the impedance phase data was set to 1.4324°. The initial model for 3-D inversion of MT data used units of 100 Ωm. The inversion results were then used to reconstruct an impression model (Ye T et al., 2013). We used the revised initial model and the apparent resistivity (R_{xy} and R_{yx}) and impedance phase (P_{xy} and P_{yx}) data to create a second inversion. The RMS of the final result was 1.92 after 366 iterations, verifying that the revised initial model could be used reliably for 3-D inversion calculation of the BBMT and AMT data.

Next we chose the BBMT final result for the initial model and started the all-frequency-band inversion calculation for the BBMT and AMT measuring points. The inversion grid design was as follows: grids in the *x* and the *y* directions were 75 m and 100 m, respectively; the extending grids in the *x* and *y* directions numbered 10 in each direction; grid spacing was increased at a proportionality factor of 1.75. The thickness of the first layer in the *z* direction was 20 m extending down to 1700 m; each subsequent layer step from 1700 to 2200 m was 1.2 times the width of the previous layer and 1.1 times the previous step's length from 2200 to 3200 m, then 1.05 times the previous step length from 3200 to 6700 m, and finally 1.1 times the previous step length from 6700 to 16,700 m. At 16,700 to 81,700 m, the step size factor increase becomes 1.2 times. The number of inversion grids is 48 (*x*) × 109 (*y*) × 143 (*z*), for a total of 748,176 grids. The final inversion calculation uses 46 BBMT and 131 AMT measuring points. The frequency used for the inversion is 45, with frequency ranging from 0.00084

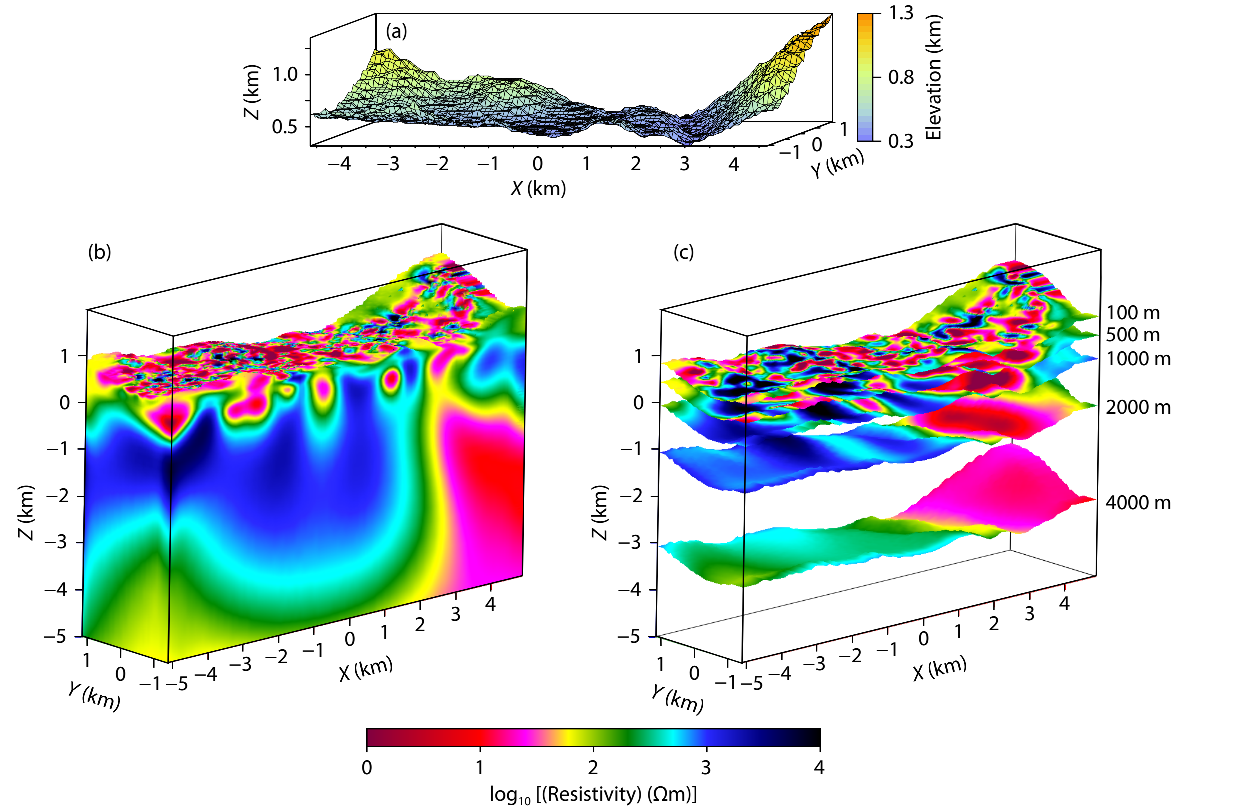

Figure 5. (a) The topography grid in study area; (b) the final 3-D resistivity model; (c) the resistivity surface graphs in the 3-D terrain framework.

to 3600 Hz. Apparent resistivity (R_{xy} and R_{yx}) and impedance phase (P_{xy} and P_{yx}) data are selected carefully for compatability with other inversion data. The error floor of the apparent resistivity was set to 5%, that of the phase data to 1.4324°.

The initial resistivity model used for 3-D inversion of combined BBMT and AMT measuring points is based on the inversion results obtained under the coarse grid condition of the BBMT data. A 3-D impression and iterative reconstruction inversion technique were employed to reduce known weaknesses of the initial model (Ye T et al., 2013). On the basis of the existing deep electrical structure model, after several inversion processes, we obtained a high-resolution 3-D electrical structure model with depth up to 5 km in the study area (Figure 5b). The RMS of the final result is 1.97 after 500 iterations. The site-by-site RMS misfit indicates that the 3-D inversion model matches the empirical observations at most sites (Figure 6).

Due to the large topographic relief in the survey area, using traditional horizontal slices would lead to a large topographic blank area, and could not show in sufficient detail the relationship between fault structure and electrical structure in the horizontal direction. Thus, this paper takes the elevation of each grid point on the surface as its reference points, intercepts the same depth from the surface at each point, and extracts the resistivity data of the same positions in order to expose in greater detail the relationship between fault structure and electrical structure, This method avoids the phenomenon of blank areas in the horizontal section. Figure 5c shows resistivity surface models for 3-D environment depths of 100 m, 500 m, 1000 m, 2000 m, and 4000 m.

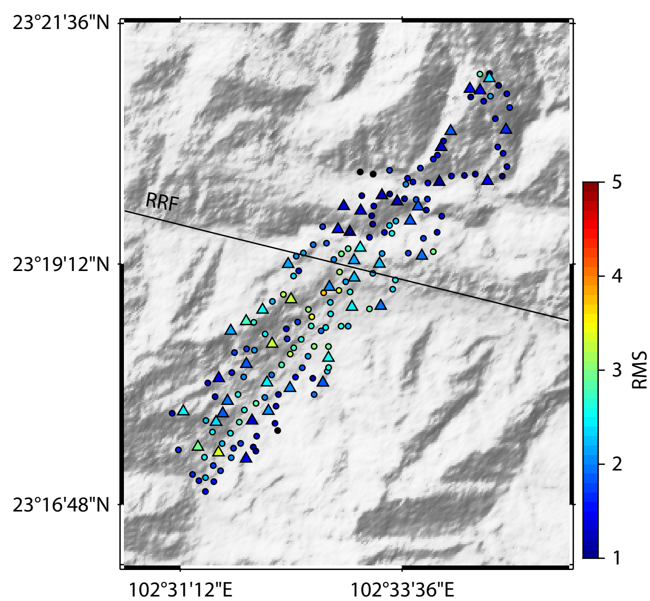

Figure 6. Site-by-site RMS misfit distribution of the 3-D inversion. Triangle points indicate BBMT sites; circle points indicate AMT sites. Colors of points indicate degree of misfit.

5.2 Resistivity Models

Figure 7 shows the 3-D resistivity surface graphs at different depths that are parallel to the terrain. The section direction is NE50°. From the resistivity results for surfaces from 100 m to 700 m it can be seen that the shallow electrical structure characteristics of the study area are extremely complex, with high and

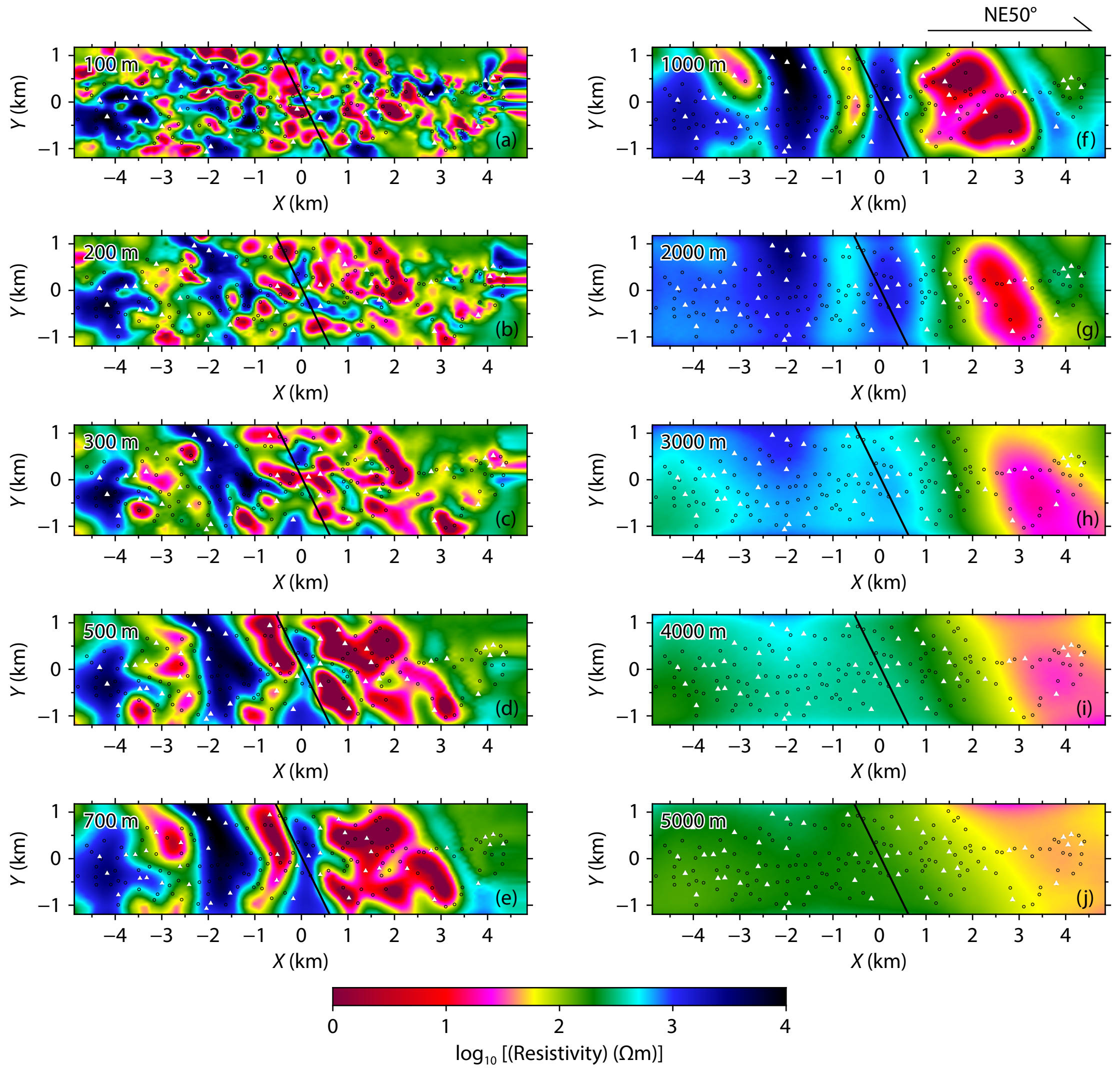

Figure 7. The resistivity surface graphs at consistent depths of (a) 100 m, (b) 200 m, (c) 300m, (d) 500 m, (e) 700 m, (f) 1000 m, (g) 2000 m, (h) 3000 m, (I) 4000 m, and (j) 5000 m. White triangles indicate BBMT sites; black hollow dots indicate AMT sites; black lines indicate fault locations.

low resistivity alternating, and evidence of a relatively significant electrical boundary fracture. The southwest side exhibits high resistivity characteristics, resistivity values greater than 1000 Ωm, which suggest that this is a Proterozoic metamorphic rock. The northeast side is characterized by low resistivity, values less than 25 Ωm, suggesting that it is a Cenozoic sandstone. In addition, a small number of relatively high conductivity layers can be detected within 500 m depth of the high resistivity body in the southwest of the study area, which may be caused by local fluids.

From the resistivity surface model at 1000–4000 m, it can be seen that as underground depth increases, the scope of the high resistivity body further increases while the scale of the low resistivity body at greater depth gradually shrinks while continuing to extend toward the northeast. Unfortunately, due to limitations of data quality and resolution, at depths greater than 5000 m, the surface models have little or no ability to identify structures.

6. Verification

After the final inversion models were chosen, we carried out model reliability tests to investigate whether the main model features are constrained by the measured BBMT+AMT data. The tests examined the robustness of the key structures in the preferred inversion model shown in Figure 8. Forward modeling simulations were systematically conducted on three critical anomalous bodies (C1, R1, and R2) by substituting their inversion-derived resistivity values with those of the surrounding media. To quantify differences in the RMS misfits between baseline model and modified model, we used a relative error parameter, ΔRMS (Garcia et al., 2015), defined as:

$$\Delta \mathrm{RMS} = \frac{\mathrm{RMS}_1 - \mathrm{RMS}_0}{\mathrm{RMS}_0} \times 100\%, \tag{1}$$

where RMS_0 is the RMS of the baseline model which is the final model and RMS_1 is the RMS of the modified model. By the definition in Equation (1), a positive ΔRMS value means a worsening of data fitting compared to the baseline model, whereas a negative ΔRMS value indicates an improved data fitting. Figure 8a represents the baseline model of the slice at the elevation of 0 m. Figures 8b–d exhibit the modified models of C1, R1, and R2 at the elevation of 0 m. Figure 8e–g presents RMS misfit values at the AMT and BBMT sites in the three tests.

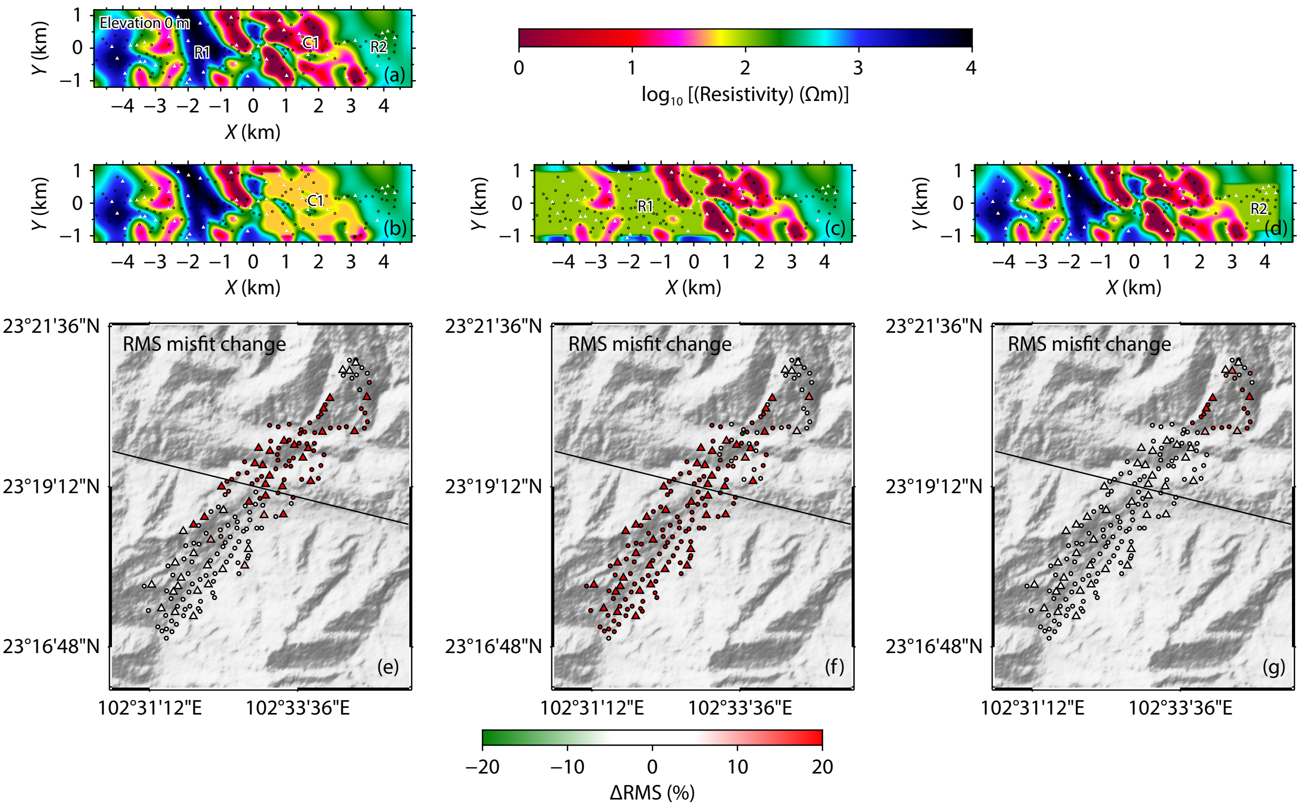

Figure 8. An update map for the three tests discussed in the text. The three starting models for the testing are defined by removing the resistivities used in the baseline models, replacing them with resistivities measured in the immediate neighborhoods of each anomaly. (a) The baseline electrical resistivity model of the slice at the elevation of 0 m. (b–d) The corresponding modified electrical resistivity models for each anomaly, C1, R1, and R2, at the elevation of 0 m. (e–g) The corresponding RMS misfit changes observed in the three test models presented in (b–d).

The anomaly C1 has a resistivity of from 1 to 10 Ωm between 2 km and 5 km depth in the Red river valley. In the C1 test, a resistivity value close to 50 Ωm was substituted for these lower values, based on the resistivity measured in the area surrounding C1. The resulting test map (Figure 8e) shows that forward modeling of the perturbed (test) model worsens the data fit for the BBMT and AMT land sites located above and close to the C1 anomaly. Similar results were found in the case of the other anomalies. The anomaly R1 has a resistivity of from 500 to 2000 Ωm between 1.7 km and 4.6 km depth in the southwest of the study area. Here we substituted a 100 Ωm half space, again using a value suggested by the surrounding resistivity. The R1 map (Figure 8f) again shows that forward modeling of the test model worsens the associated BBMT and AMT data fits. The anomaly R2 has a resistivity of from 1 to 10 Ωm between 1.7 km and 3.4 km depth in the northeast of the study area. Substituting a resistivity value close to 100 Ωm, based again on values measured near the anomaly, again worsened the data fit of neighboring BBMT and AMT sites (Figure 8g). These results confirm that the model results do indeed benefit from inclusion of the BBMT and AMT data collected at the anomalies.

7. Discussion

7.1 The Shallow Fault Geometric Distribution

Figure 9 shows that three electrical profiles traverse the RRF in the Dazhai region, in which Figure 9a is the location of the L1, L2, and L3 profiles. Generally, the electrical structures displayed in the three electrical profiles are similar, showing two high and one low electrical resistivity characteristics, and sporadic low resistivity bodies are developed locally (Figure 9b–d). The blocks on both sides of the RRF are characterized by high and low resistivity distribution. The southwest side of the measurement area is the R1 with resistivity >1000 Ωm; the surface corresponds to the Ailao mountain Proterozoic metamorphic rock with a thickness of more than 3 km. The northeast side of the R1 is the C1 with resistivity <10 Ωm; the C1 is spread laterally about 2 km and has a thickness of more than 5 km. It is presumed to be the Cenozoic sandstone (Figure 2) developed by faulting in the Red River valley. The northeast side of the C1 is also a set of R2 with resistivity >1000 Ωm. The surface corresponds to Paleozoic metamorphic rock and Mesozoic mudstone. The C1 located in the Red River valley is probably affected by old local geological bodies, which leads to its uneven distribution. R2 also dominates the side of the C1 near the mountain to the northeast. Although the electrical characteristics of the Proterozoic strata are similar to those of Ailao mountain Proterozoic strata located in the southwest of the survey area, these two sets of strata were formed in different tectonic evolution periods of the southern segment of the RRF.

The Dazhai village delineates a distinct boundary fault zone with high and low resistivity bodies in the southern segment of the RRF. It corresponds to the location of surface active faults and the

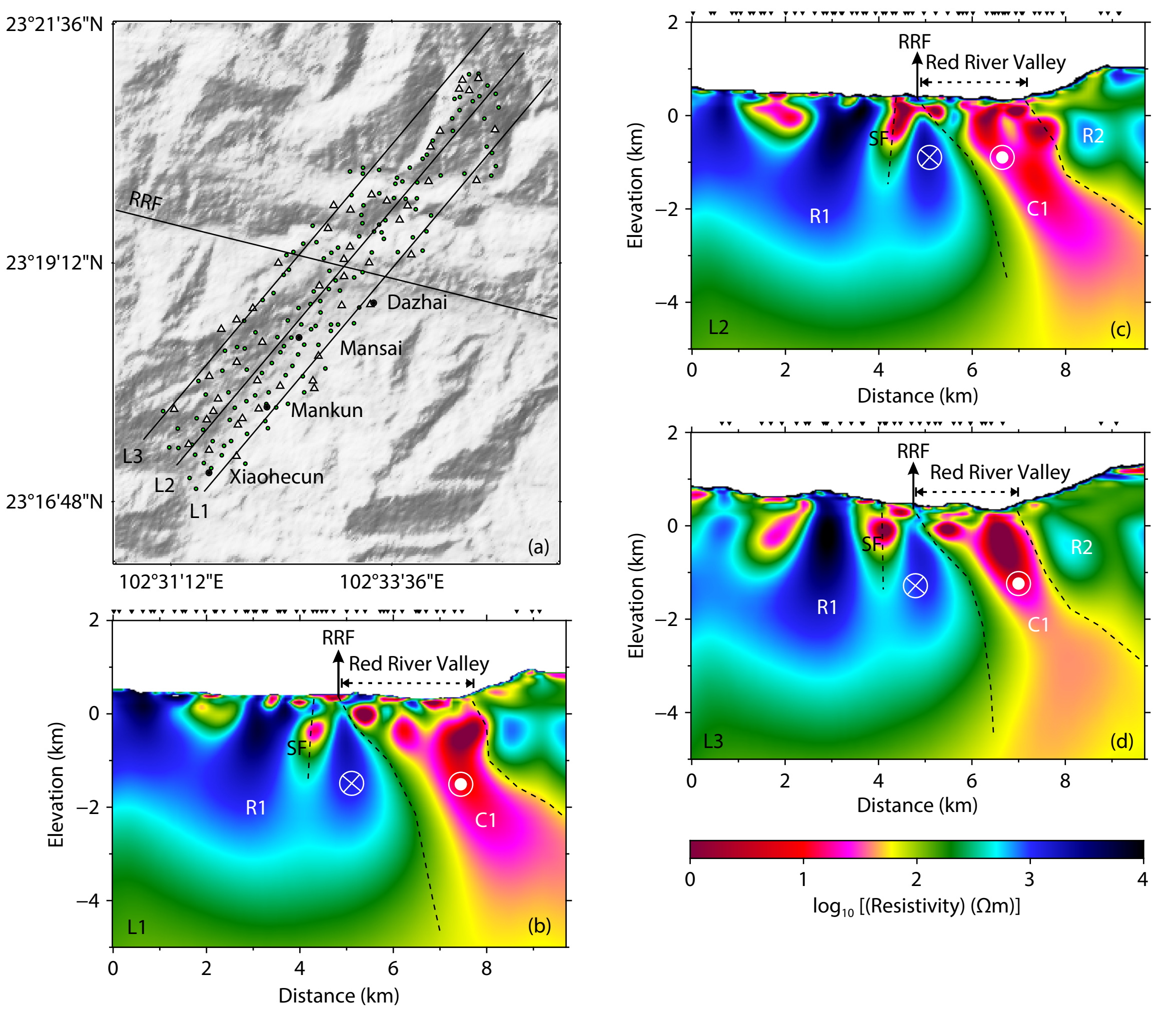

Figure 9. (a) Overview of the RRF study region. White triangles indicate locations of BBMT sites; green solid dots indicate AMT sites. The three black lines show how the study region is oriented relative to the RRF fault. (b–d) Electrical resistivity model profiles at different depths at the study region; SF indicates location of the Secondary Fault; black arrow points to the main fault location.

Red River, indicating that the tectonic features of the Dazhai area are extremely complex, with multiple secondary faults existing. The results show that the geometric form of the southern segment of the RRF is characterized by a northeastward dip in-depth and a low-resistivity channel with a width of about 2 km. The geometric form of the southern segment of the RRF is mainly characterized by a shallow, nearly vertical (high angle) extension and a deep northeastward dip. It is consistent with the general northeastward direction of the fault revealed by the surface survey results (Zhang JJ et al., 2006). However, near the old Ailao mountain structure (high resistivity zone), southwest-inclined or nearly vertical secondary faults, too, are found in the shallow side; these secondary faults extend to a depth of about 2–3 km and ultimately disappear in high resistivity bodies. The electrical structural profile across the southern segment of the RRF thus suggests that although these nearly vertical or southwest dipping secondary faults exhibit some geometric extension into depth, they do not completely penetrate the high resistivity terrane.

It should be noted that a wide angle reflection/refraction seismic profile developed around the RRF (Wang FY et al., 2014; Chen SW et al., 2016) revealed that the RRF is SW dip in depth, indicating that the geometric extension characteristics of the southern segment of the RRF in depth may be inconsistent with the tendency of the shallow section. Due to the significant differences in geological characteristics along different sections of the RRF zone, the authors believe that the electrical structure detected in this paper directly reflects the geometric shape of the southern segment of the RRF zone within 5 km from the surface. However, our results cannot accurately judge whether the deep extension characteristics of the RRF below 5 km are likely to be inclined to the southwest. Li R et al. (2014) conducted magnetotelluric exploration research on the RRF, but due to the resolution problem the deep geometric extension characteristics of the southern segment of the RRF were not clearly indicated. Therefore, the deep geometry of the southern segment of the RRF needs to be analyzed using geophysical methods with higher precision.

7.2 Seismic Activity

Seismic activity is direct evidence of the movement deformation of a fault. According to the existing seismic activity records, the seismic activity in the southern segment of the RRF is weak. The electrical structure reveals that the measured area has a low resistivity zone spreading transverse about 2 km; it plays an excellent lubricating effect on the relative movement of the blocks on both sides of the fault zone, resulting in the plastic deformation of the shear force acting on the fault zone. Eventually, it releases energy in the form of creep. Guo SM et al. (2001) also believed that the southern segment of the RRF was characterized by creep deformation. GPS data reveal that the southern segment of the RRF is in a state of creep at a depth of 2–5 km (Li N et al., 2019). The minor seismic activities in the southern segment of the RRF zone are mainly concentrated at a depth of 5 to 22 km, demonstrating a relatively weak degree of locking and suggesting that the possibility of a large earthquake in the short term is unlikely. However, these phenomena cannot exclude the seismic risk of the southern segment of the RRF. Li X et al. (2016) proposed that the southern segment of the RRF has had many earthquakes since the Holocene by using the results of the exploratory trough, but we still lack quantitative paleo-seismic research results. Therefore, more high-quality work and persuasive evidence are needed to estimate seismic risk in the southern segment of the RRF with greater confidence.

Dilatation rate is a crucial parameter of structural deformation in underground media. Figure 10a displays the distribution of dilatation rates in the southern segment of the RRF and its adjacent areas (Wang M and Shen ZK, 2020). We suggest that the southern segment of the RRF is in a tectonic deformation environment of regional decompression. Based on the electrical structural characteristics of the southern segment of the RRF at a depth of 5 km (Figure 10b), we speculate that the upper crust seismogenic layer located at a depth of 10–15 km on the side of Ailao mountain is likely to have a block with high resistivity characteristics wedged into the RRF (high conductor) in the northeast direction, and the wedged high resistivity body can accumulate a certain intensity of stress under the action of regional stress. Such a continuous concentration of stress can lead to fault movement causing shear rupture of the high resistivity wedged body, and finally triggering strong earthquakes, a sequence that accords with the tectonic activity characteristics of the rigid flexible wedge inlay model (Ye T et al., 2021). This reasoning suggests that the southern segment of the RRF has the prerequisites for strong earthquakes. We also posit that this area is situated within a low resistivity zone formed by alluvial deposits of the Red River valley, where active structural layers with paleo-seismic records are likely to be present. But our current knowledge of the electrical structure, due to the limited distribution of magnetotelluric measurement points and the insignificant differences so far detected in electrical conductivity between fault-dislocated structural layers, is too limited to allow identification of these hidden geological structures. Future work should focus on comprehensive analysis that includes additional data from drilling and from surveys of active geological faults.

8. Conclusion

We present a model of the shallow crustal electrical structure in the RRF (Dazhai village) and adjacent region, based on 3-D BBMT+AMT array survey images. The following three points are the most significant:

(1) The electrical structure of this southern segment of the RRF zone reveals structural complexity in the shallow part, similar to qualitative analysis results of impedance tensor decomposition, showing that electrical characteristics from southwest to northeast vary from high, to low, and then high. Taking the RRF as the boundary, the high resistivity body revealed on the southwest side of the fault zone is inferred to be the Ailao mountain Proterozoic old tectonic stratum. The high conductive layer of width 2 km near the northeast side of the fault zone corresponds to the Cenozoic stratum, a dynamic geological process; in a significant transition, this high conductive layer transforms into the Mesozoic stra-

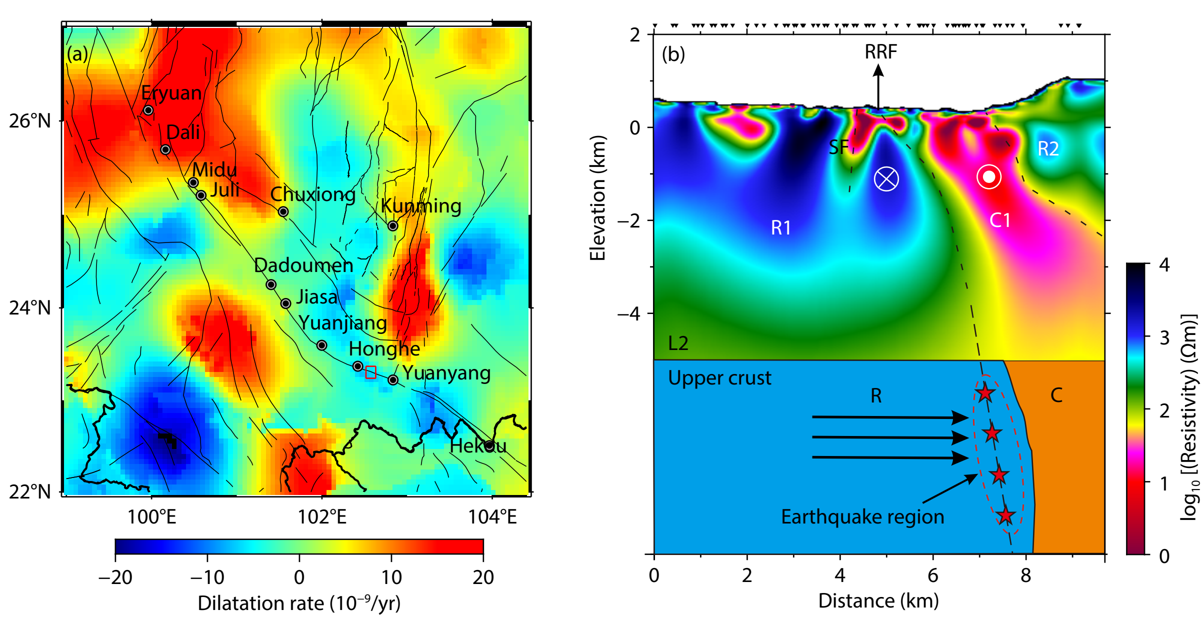

Figure 10. (a) Dilatation rate distribution in the southern segment of the RRF and adjacent region (from Wang M and Shen ZK, (2020). (b) Seismogenic model of the deep structure in the study region (indicated by red box in Figure 1b); red stars indicate location of the fault rupture or earthquake epicenter.

tum in the northeast direction.

(2) The study area described above is a significant boundary fault zone with high and low resistivity, in which the geometry of the main fault zone is characterized by an extension and distribution that inclines northeastward at a depth of 5 km. There are also several nearly vertical or southwest dip secondary faults near the Ailao Mountain old structural strata, but these secondary faults extend no more than 3 km deep, and finally disappear in the high resistivity body.

(3) A high conductor with a transverse width of 2 km appears in a low resistivity zone formed by alluvia of the Red River valley on the northeast side of the southern segment of the RRF zone, and a new active structural layer is likely to have developed inside the high conductor. However, the precise location of the fault cannot be accurately delineated based on the electrical structure. It is thus imperative to integrate field geological survey in further research.

Acknowledgments

This work was supported by research grants from the National Institute of Natural Hazards, MEMC (ZDJ2020-13), the National Natural Science Foundation of China (42174093), and the Innovation Team Project from National Institute of Natural Hazards, MEMC (2023-JBKY-59). The work of drawing the rose graph, the bi-orthogonal diamond graph and matching test of apparent resistivity and phase data was accomplished by relying on the MTP software developed by our research group. Most figures in this paper were drawn with the help of Generic Mapping Tools Version 6 (Wessel et al., 2019). Thanks to Beijing Super Cloud Center for providing technical support for the inversion calculation of this paper.

References

Allen, C. R., Gillespie, A. R., Han, Y., Sieh, K. E., Zhang, B. C., and Zhu, C. N. (1984). Red River and associated faults, Yunnan Province, China: Quaternary geology, slip rates, and seismic hazard. *GSA Bull.*, *95*(6), 686–700. https://doi.org/10.1130/0016-7606(1984)95<686:RRAAFY>2.0.CO;2

Becken, M., Ritter, O., Bedrosian, P. A., and Weckmann, U. (2011). Correlation between deep fluids, tremor and creep along the central San Andreas fault. *Nature*, *480*(7375), 87–90. https://doi.org/10.1038/nature10609

Cagniard, L. (1953). Basic theory of the magneto-telluric method of geophysical prospecting. *Geophysics*, *18*(3), 605–635. https://doi.org/10.1190/1.1437915

Cai, J. T., Chen, X. B., and Zhao, G. Z. (2010). Refined techniques for data processing and two-dimensional inversion in magnetotelluric I: Tensor decomposition and dimensionality analysis. *Chinese J. Geophys. (in Chinese)*, *53*(10), 2516–2526. https://doi.org/10.3969/j.issn.0001-5733.2010.10.025

Cai, J. T., Chen, X. B., Dong, Z. Y., Zhan, Y., Liu, Z. Y., Cui, T. F., and Jiang, F. (2023). Three-dimensional electrical structure beneath the epicenter zone and seismogenic setting of the 1976 Ms7.8 Tangshan earthquake, China. *Geophys. Res. Lett.*, *50*(14), e2022GL102291. https://doi.org/10.1029/2022GL102291

Caldwell, T. G., Bibby, H. M., and Brown, C. (2004). The magnetotelluric phase tensor. *Geophys. J. Int.*, *158*(2), 457–469. https://doi.org/10.1111/j.1365-246X.2004.02281.x

Chen, S. W., Wang, B. S., Tian, X. F., Wang, F. Y., Liu B. F., and Li, L. (2016). Crustal structure from Yunxian-Ninglang wide-angle seismic reflection and refraction profile in northwestern Yunnan, China. *Seismol. Geol. (in Chinese)*, *38*(1), 91–106. https://doi.org/10.3969/j.issn.0253-4967.2016.01.007

Chen, X. B., Cai, J. T., Wang, L. F., and Ye, T. (2014). Refined techniques for magnetotelluric data processing and two-dimensional inversion (IV): Statistical image method based on multi-site, multi-frequency tensor decomposition. *Chinese J. Geophys. (in Chinese)*, *57*(6), 1946–1957. https://doi.org/10.6038/cjg20140625

Egbert, G. D., and Kelbert, A. (2012). Computational recipes for electromagnetic inverse problems. *Geophys. J. Int.*, *189*(1), 251–267. https://doi.org/10.1111/j.1365-246X.2011.05347.x

Gao, J., Zhang, H. J., Zhang, S. Q., Xin, H. L., Li, Z. W., Tian, W., Bao, F., Cheng, Z. P., Jia, X. F., and Fu, L. (2020). Magma recharging beneath the Weishan volcano of the intraplate Wudalianchi volcanic field, northeast China, implied from 3-D magnetotelluric imaging. *Geology*, *48*(9), 913–918. https://doi.org/10.1130/g47531.1

Garcia, X., Seillé, H., Elsenbeck, J., Evans, R. L., Jegen, M., Hölz, S., Ledo, J., Lovatini, A., Marti, A., … Ranero, C. R. (2015). Structure of the mantle beneath the Alboran Basin from magnetotelluric soundings. *Geochem. Geophys. Geosyst.*, *16*(12), 4261–4274. https://doi.org/10.1002/2015GC006100

Guo, S. M., Ji, F. J., Xiang, H. F., and Dong, X. Q.(2001). *Red River Activity Fault* (pp. 89–108) (in Chinese). Beijing: China Ocean Press.

Hao, T. Y., Jiang, W. W., Xu, Y., Qiu, X. L., Liu, J. H., Dai, M. G., Xu, Y., Huang, Z. X., and Song, H. B. (2005). Geophysical research on deep structure feature in study region of Red River fault zone. *Prog. Geophys. (in Chinese)*, *20*(3), 584–593.

Ji, S. C., Wang, Q., Sun, S. S., Xu, Z. Q., and Li, H. B. (2008). Continental extrusion and seismicity in China. *Acta Geol. Sin. (in Chinese)*, *82*(12), 1644–1667. https://doi.org/10.3321/j.issn:0001-5717.2008.12.003

Kelbert, A., Meqbel, N., Egbert, G. D., and Tandon, K. (2014). ModEM: A modular system for inversion of electromagnetic geophysical data. *Comput. Geosci.*, *66*, 40–53. https://doi.org/10.1016/j.cageo.2014.01.010

Li, N., Kang, S., and Zhu, L. Y. (2019). Study on present-day locking and seismic hazard of the Red River fault zone based on GPS data. *J. Geod. Geodyn. (in Chinese)*, *39*(7), 700–705. https://doi.org/10.14075/j.jgg.2019.07.007

Li, R., Tang, J., Dong, Z. Y., Xiao, Q. B., and Zhan, Y. (2014). Deep electrical conductivity structure of the southern area in Yunnan Province. *Chinese J. Geophys. (in Chinese)*, *57*(4), 1111–1122. https://doi.org/10.6038/cjg20140409

Li, X., Ran, Y. K., Chen, L. C., Wang, H., Yu, J., Zhang, Y. Q., and Xie, Y. Q. (2016). The Holocene seismic evidence on southern segment of the Red River fault zone. *Seismol. Geol. (in Chinese)*, *38*(3), 596–604. https://doi.org/10.3969/j.issn.0253-4967.2016.03.007

Liu, L. J., and Hasterok, D. (2016). High-resolution lithosphere viscosity and dynamics revealed by magnetotelluric imaging. *Science*, *353*(6307), 1515–1519. https://doi.org/10.1126/science.aaf6542

Liu, Z. Y., Chen, X. B., Cai, J. T., Cui, T. F., Zhao, G. Z., Tang, J., and Ouyang, B. (2022). The design and application of toPeak: A three-dimensional magnetotelluric inversion cloud computing system. *Seismol. Geol. (in Chinese)*, *44*(3), 802–820. https://doi.org/10.3969/j.issn.0253-4967.2022.03.015

Liu, Z. Y., Chen, X. B., Cai, J. T., Zhang, Y. Y., and Wang, P. J. (2023). A magnetotelluric multi-scale and multi-period exploration method. *Chinese J. Geophys. (in Chinese)*, *66*(9), 3761–3773. https://doi.org/10.6038/cjg2023Q0855

Liu, Z. Y., Kelbert, A., and Chen, X. B. (2024). 3D magnetotelluric inversion with arbitrary data orientation angles. *Comput. Geosci.*, *188*, 105596. https://doi.org/10.1016/j.cageo.2024.105596

Parker, R. L., and Booker, J. R. (1996). Optimal one-dimensional inversion and bounding of magnetotelluric apparent resistivity and phase measurements. *Phys. Earth Planet. Inter.*, *98*(3-4), 269–282. https://doi.org/10.1016/S0031-9201(96)03191-3

Replumaz, A., Lacassin, R., Tapponnier, P., and Leloup, P. H. (2001). Large river offsets and Plio-Quaternary dextral slip rate on the Red River fault (Yunnan, China). *J. Geophys. Res.: Solid Earth*, *106*(B1), 819–836. https://doi.org/10.1029/2000JB900135

Schoenbohm, L. M., Burchfiel, B. C., Chen, L. Z., and Yin, J. Y. (2006). Miocene to present activity along the Red River fault, China, in the context of continental extrusion, upper-crustal rotation, and lower-crustal flow. *GSA*

Bull., *118*(5-6), 672–688. https://doi.org/10.1130/B25816.1

Sun, X. Y., Zhan, Y., Unsworth, M., Egbert, G., Zhang, H. P., Chen, X. B., Zhao, G. Z., Sun, J. B., Zhao, L. Q., … Han, J. (2020). 3-D magnetotelluric imaging of the easternmost Kunlun fault: insights into strain partitioning and the seismotectonics of the Jiuzhaigou M_s7.0 earthquake. *J. Geophys. Res.: Solid Earth*, *125*(5), e2020JB019731. https://doi.org/10.1029/2020jb019731

Tapponnier, P., Lacassin, R., Leloup, P. H., Schärer, U., Zhong, D. L., Wu, H. W., Liu, X. H., Ji, S. C., Zhang, L. S., and Zhong, J. Y. (1990). The Ailao Shan/Red River metamorphic belt: Tertiary left-lateral shear between Indochina and South China. *Nature*, *343*(6257), 431–437. https://doi.org/10.1038/343431a0

Tapponnier, P., Xu, Z. Q., Roger, F., Meyer, B., Arnaud, N., Wittlinger, G., and Yang, J. S. (2001). Oblique stepwise rise and growth of the Tibet plateau. *Science*, *294*(5547), 1671–1677. https://doi.org/10.1126/science.105978

Tikhonov, A. N. (1950). On determining electrical characteristics of the deep layers of the Earth's crust. *Doklady*, *73*(2), 295–297.

Unsworth, M. J., Jones, A. G., Wei, W., Marquis, G., Gokarn, S. G., and Spratt, J. E. (2005). Crustal rheology of the Himalaya and Southern Tibet inferred from magnetotelluric data. *Nature*, *438*(7064), 78–81. https://doi.org/10.1038/nature04154

Wang, F. Y., Pan, S. Z., Liu, L., Liu, B. F., Zhang, J. S., Deng, X. G., Ma, C. J., and Zhang, C. J. (2014). Wide angle seismic exploration of Yuxi-Lincang profile—The research of crustal structure of the Red River fault zone and southern Yunnan. *Chinese J. Geophys. (in Chinese)*, *57*(10), 3247–3258. https://doi.org/10.6038/cjg20141013

Wang, M., and Shen, Z. K. (2020). Present-day crustal deformation of continental China derived from GPS and its tectonic implications. *J. Geophys. Res.: Solid Earth*, *125*(2), e2019JB018774. https://doi.org/10.1029/2019JB018774

Wang, M. C., Liu, Z. F., and Luo, R. J. (2024). Stress triggering effect on the 2022 Honghe M_S5.0 earthquake with historical strong earthquakes. *Geod. Geodyn.*, *15*(2), 107–113. https://doi.org/10.1016/j.geog.2023.07.008

Wen, X. Z., Ma, S. L., Fang, L. H., Liang, M. J., Du, F., Long, F., and Zhao, X. Y. (2022). Complex structural fault system and distributed deformation across the Big Bend of the Red River fault, Yunnan, China. *Phys. Earth Planet. Inter.*, *333*, 106942. https://doi.org/10.1016/j.pepi.2022.106942

Wessel, P., Luis, J. F., Uieda, L., Scharroo, R., Wobbe, F., Smith, W. H. F., and Tian, D. (2019). The generic mapping tools version 6. *Geochem. Geophys. Geosyst.*, *20*(11), 5556–5564. https://doi.org/10.1029/2019GC008515

Xu, X. W., Han, Z. J, Yang, X. P., Zhang, S.M. Yu, G. H., Zhou, B. G, Li, F., Ma, B. Q., Chen, G. H., and Ran, Y. K. (2016). *Seismotectonic Map in China and its Adjacent Regions* (in Chinese). Beijing: Seismological Press.

Xu, X. W., Wu, X. Y., Yu, G. H., Tan, X. B., and Li, K. (2017). Seismo-geological signatures for identifying $M \geq 7.0$ earthquake risk areas and their premilimary application in mainland China. *Seismol. Geol. (in Chinese)*, *39*(2), 219–275. https://doi.org/10.3969/j.issn.0253-4967.2017.02.001

Xu, Z. Q., Yang, J. S., Li, H. B., Ji, S. C., Zhang, Z. M., and Liu, Y. (2011). On the tectonics of the India-Asia collision. *Acta Geol. Sin. (in Chinese)*, *85*(1), 1–33. https://doi.org/10.1111/j.1755-6724.2011.00375.x

Yamaya, Y., Suzuki, Y., Murata, Y., Okamoto, K., Watanabe, N., Asanuma, H., Hase, H., Ogawa, Y., Mogi, T., … Uchida, T. (2022). 3-D resistivity imaging of the supercritical geothermal system in the Sengan geothermal region, NE Japan. *Geothermics*, *103*, 102412. https://doi.org/10.1016/j.geothermics.2022.102412

Ye, T., Chen, X. B., and Yan, L. J. (2013). Refined techniques for data processing and two-dimensional inversion in magnetotelluric (III): using the impressing method to construct starting model of 2D magnetotelluric inversion. *Chinese J. Geophys. (in Chinese)*, *56*(10), 3596–3606. https://doi.org/10.6038/cjg20131034

Ye, T., Chen, X. B., Huang, Q. H., and Cui, T. F. (2021). Three-dimensional electrical resistivity structure in focal area of the 2021 Yangbi M_s6.4 Earthquake and its implication for the seismogenic mechanism. *Chinese J. Geophys. (in Chinese)*, *64*(7), 2267–2277. https://doi.org/10.6038/cjg2021O0523

Ye, T., Chen, X. B., Liu, Z. Y., Wang, P. J., Dong, Z. Y., Cui, T. F., Jiang, F., Cai, J. T., Zhang, Y. Y., … Xie, X. B. (2022). A magnetotelluric study of 3D electrical resistivity structure underneath the southern segment of the Red River fault zone, South China. *J. Asian Earth Sci.*, *225*, 105056. https://doi.org/10.1016/j.jseaes.2021.105056

Yu, N., Unsworth, M., Wang, X. B., Li, D. W., Wang, E. C., Li, R. H., Hu, Y. B., and Cai, X. L. (2020). New insights into crustal and mantle flow beneath the Red River Fault zone and adjacent areas on the southern margin of the Tibetan Plateau revealed by a 3-D magnetotelluric study. *J. Geophys. Res.: Solid Earth*, *125*(10), e2020JB019396. https://doi.org/10.1029/2020jb019396

Zhang, J., Chen, X. B., Yin, X. K., Zhao, S. W., Ye, T., Xu, Z. X., Cai, J. T., Wang, P. J., Zhang, Y. Y., and Liu, Z. Y. (2022). 3-D AMT array exploration in the Selaha fault and adjacent area. *Earth Sci. (in Chinese)*, *47*(3), 856–866. https://doi.org/10.3799/dqkx.2022.060

Zhang, J. G., Huangfu, G., Xie, Y. Q., Trinh, P. T., and Liu, N. (2009). Study on the activity of Red River fault in Vietnam. *Seismol. Geol. (in Chinese)*, *31*(3), 389–400. https://doi.org/10.3969/j.issn.0253-4967.2009.03.002

Zhang, J. J., Zhong, D. L., Sang, H. Q., and Zhou, Y. (2006). Structural and geochronological evidence for mul-tiple episodes of deformation since Paleocene along the Ailao Shan-Red River shear zone, southeastern Asia. *Chinese J. Geol. (in Chinese)*, *41*(2), 291–310.

Zhang, P. Z., Deng, Q. D., Zhang, G. M., Ma, J., Gan, W. J., Min, W., Mao, F. Y., and Wang, Q. (2003). Active tectonic blocks and strong earthquakes in the continent of China. *Sci. China Ser. D: Earth Sci.*, *46*(2), 13–24. https://doi.org/10.1360/03dz0002